PLATE TECTONICS

Low-frequency earthquakes track the motion of a captured slab fragment

David R. Shelly[1]*, Amanda M. Thomas[2], Kathryn Z. Materna[3], Robert J. Skoumal[4]

Accurate tectonic models are essential for assessing seismic hazard and fault interactions. However, the plate configuration at the complex Mendocino triple junction, where the San Andreas Fault and the Cascadia subduction zone meet, remains uncertain. We analyzed fault slip associated with a recently identified zone of tectonic tremor and low-frequency earthquakes (LFEs) near the southern edge of the subducting Gorda slab. Based on tidal sensitivity and P-wave first motions, we show that the LFEs are generated by dipping, strike-slip motion. This suggests that a former Farallon slab fragment, now captured by the Pacific plate, is translating northward beneath westernmost North America. This geometry effectively extends the slab interface fault, challenging prevailing interpretations of slab window formation and creating a potential unaccounted earthquake hazard in this region.

With the advent of plate tectonics theory came the recognition that the behavior of triple junctions, where three tectonic plates meet, is central to understanding the evolution of the present-day plate configuration (*1*, *2*). Along the west coast of Northern California, the Mendocino triple junction marks the convergence of the Pacific, North American, and Gorda (southern Juan de Fuca) plates (*3*, *4*) and forms the boundary between the strike-slip San Andreas Fault system and the Cascadia subduction zone (Fig. 1). Although often idealized as a single point, in three dimensions, the triple junction is a broad, complex region. It encompasses a network of major and minor faults that exhibit high rates of seismicity and accommodate both seismic and aseismic deformation across the three interacting plate boundaries, with high rates of deformation extending well into the Gorda plate (*5*). The triple junction at the northern end of Cascadia is also seismically active and may be similarly complex (*6*–*8*).

The nature of the transition between the Cascadia subduction zone and the San Andreas Fault system has long been debated (*4*, *9*). Despite extensive study, uncertainty persists regarding fundamental tectonic features, particularly the nature of the southern edge of the Gorda subduction. One model holds that a slab gap (window) has formed at the southern edge of the northward-migrating, subducting Gorda plate, leading to shallow asthenospheric upwelling (*9*–*14*). A contrasting model proposes that this region is underlain by a subducted Farallon slab fragment captured by the Pacific plate and sharing its northward motion (*15*). In the latter scenario, this captured slab, called the Pioneer Fragment (*16*, *17*), would lie beneath the North American plate crust and track the northward motion of the southern edge of Gorda subduction at depth, preventing formation of slab window in this location. However, no evidence has directly constrained the modern-day kinematics.

[1]US Geological Survey, Geologic Hazards Science Center, Golden, CO, USA. [2]Department of Earth and Planetary Sciences, University of California, Davis, CA, USA. [3]Department of Geological Sciences, University of Colorado Boulder, Boulder, CO, USA. [4]US Geological Survey, Earthquake Science Center, Moffett Field, CA, USA. ***Corresponding author. Email: dshelly@usgs.gov**

Tremor and low-frequency earthquakes (LFEs) might provide such evidence. Tremor is a low-amplitude, long-duration seismic signal first identified in the early 2000s (*18*), which is associated with slow slip events downdip of the seismogenic zone in subduction zones (*19*, *20*). LFEs are very small individual earthquakes with rapid recurrence that form the longer-duration tremor (*21*–*23*). LFEs are often detected using matched-filter analysis, with events identified by a given waveform template considered a "family" of events. Although tremor frequently has large location and depth uncertainties, LFE source locations can be determined more accurately by identification of the *P* and *S* phases, often on stacked records combining many LFE detections (*24*). LFE and tremor activity worldwide dominantly occurs on major plate-bounding faults (*25*).

An anomalous zone of tremor, offset 50 to 100 km westward of the main band of the Cascadia tremor, was identified by Wech (*26*). Shelly *et al.* (*27*) identified and located 27 families of constituent LFEs in this zone, showing that they aligned along a zone at 22 to 29 km depth dipping ~45° toward the north-northeast, extending eastward and downdip from a neighboring zone of persistent microseismicity ($M < 3$) (Fig. 1). Given the association with major plate-bounding faults and the short (~2-day) recurrence times, Shelly *et al.* (*27*) argued that these Mendocino LFEs likely reflected slip on a high-rate plate-bounding fault, perhaps at the southern edge of Cascadia subduction. However, that study was unable to constrain the sense of slip occurring in the LFEs, leaving unanswered fundamental questions as to the nature of this boundary and its associated tectonics.

Plausible arguments could be made for various orientations of LFE slip, each with distinct tectonic implications (Fig. 2). LFEs might reflect slip between the Gorda slab and the North American plate crust at the edge of a slab window, leading to normal faulting on a structure defined by LFE hypocentral alignment (here determined as strike = 293°, dip = 48°; see the materials and methods). By contrast, if the Pioneer Fragment captured-slab hypothesis is correct, then we might observe relative motion between the Pacific and Gorda plates, for which we would expect right-lateral strike-slip motion on the LFE-defined fault. Finally, it is conceivable that the Pioneer Fragment has been captured by the Pacific plate but that the North American crust lies to the north of the LFEs, leading to oblique reverse and right-lateral strike-slip faulting to accommodate relative motion between the Pacific and North American plates (Fig. 2). The actual faulting orientation, if it could be determined, would distinguish between these distinctly different tectonic scenarios.

To address this uncertainty, we performed two complementary analyses aimed at constraining the orientation of fault slip and the tectonic significance of Mendocino LFE activity.

Focal mechanism analysis

We computed a composite first-motion focal mechanism for the LFE families. Because low signal-to-noise for these LFEs usually precludes the unambiguous determination of P-wave first motions, even on stacked records, we developed a strategy based on a comparison of P-wave arrivals with nearby earthquakes of known polarity (*28*, *29*) (see the materials and methods). These nearby earthquakes are located within a zone of persistent seismicity at ~22 km depth (*3*, *30*, *31*) with diverse focal mechanisms, which has previously been referred to as the "Garberville swarm" (*32*) (Fig. 1).

The resulting focal mechanism is shown in Fig. 2. The northeast-dipping nodal plane (strike = 292°, dip =34°) matches very well with the orientation determined by the hypocentral alignment of the families (strike = 293°, dip = 48°), which is also similar to that previously estimated visually (strike = 290°, dip = 45°) (*27*). The focal mechanism's rake angle of 177° on this plane indicates strike-slip motion. Notably, despite the variety of mechanisms observed in the reference earthquakes (Fig. 1), none closely matched the LFE mechanism.

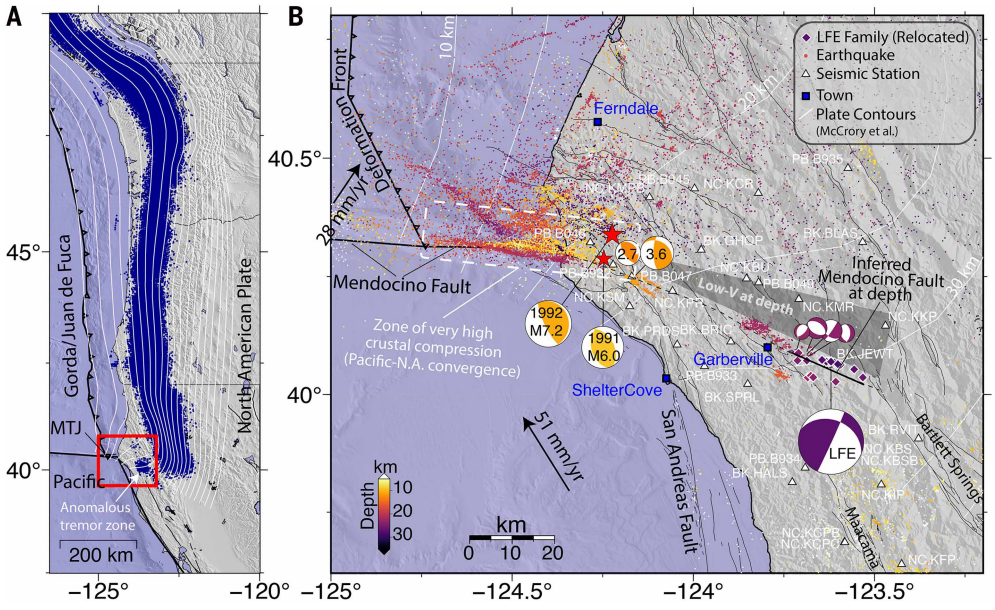

Fig. 1. Mendocino triple junction seismicity and focal mechanisms. (**A**) The Cascadia margin. White lines show subducting plate contours from McCrory *et al*. (*40*) in 5-km increments. Black lines show faults; line with triangles indicates the Cascadia subduction deformation front (western edge of the accretionary prism). Blue dots mark tremor epicenters from pnsn.org/tremor (last accessed 3 June 2025) from 1 January 2015 through 31 July 2024. Red box indicates the region shown in (B). The anomalous tremor zone studied here is highlighted. (**B**) The Mendocino triple junction region. LFE family locations are shown as white-outlined diamonds color coded by depth (*27*). Seismicity 1984 to 2021, updated from Waldhauser and Schaff (*72*), is shown as small dots and is also color coded by depth. Focal mechanisms are similarly color coded and show the 1992 M 7.2 Cape Mendocino earthquake (*47*), the 1991 M 6.0 Honeydew earthquake (ID = nc228027), and examples of other nearby thrust events, including a 2022 M 2.7 (focal mechanism, ID = nc73661611) and a 2021 M 3.6 (moment tensor, ID = nc73629686) earthquake. Also shown are the LFE composite mechanism determined in this study and a representative sample of focal mechanisms of microseismicity ($M < 3$) events used for LFE focal mechanism analysis. White triangles show the locations of seismic stations used for LFE analysis. The zone of high crustal compression (Fig. 3C) is also indicated (white dashed box). The inferred buried eastward extension of the Mendocino fault is shown as a black line near LFEs, with a dashed line connecting it to the offshore Mendocino fault. The shaded region just to the north is the nearly aseismic region of observed low P-wave velocity (low-V) at depth (*17*, *31*). Motions for the Gorda and Pacific plates (see the materials and methods) relative to the North American plate are also shown. Black lines show faults from the Quaternary Fault and Fold Database (with major fault zones are labeled), which are generally shallow faults not directly related to deeper structures. Topography and bathymetry are from Ryan *et al*. (*73*).

Tidal analysis

Strong tidal modulation of tremor and LFEs has been well documented in multiple fault zones, including the Nankai subduction zone (*33*, *34*), the Cascadia subduction zone (*35*, *36*), and the central San Andreas Fault (*37*, *38*). Because the LFE families documented by Shelly *et al*. (*27*) occur with short recurrence intervals, as opposed to being driven by large, transient slow-slip events such as those that occur farther north on the Cascadia subduction zone, we expect the LFE rate to be proportional to the tidal stress amplitude, as has been shown in other settings that host nearly continuous LFEs (e.g., the San Andreas Fault near Parkfield). The stresses imposed by tides vary according to fault and slip orientation, so we can estimate the optimal fault geometry by determining which fault orientation and sense of slip maximizes the occurrence of LFEs during positive (slip-encouraging) shear stress changes imparted by the tides. We modeled these effects to determine whether the Mendocino LFEs are also tidally modulated and the range of slip orientations consistent with this modulation (see the materials and methods).

For all families combined, we found strong tidal modulation that is broadly consistent with either normal faulting or strike-slip faulting, meaning that an excess number of LFEs occur during tidally encouraging shear stress but are inconsistent with reverse faulting (Fig. 2, C and D). For a strike of 293° and dips of 35° to 55°, we found that the strongest and most systematic modulation (i.e., the maximum slope) occurs for dip = 40°, rake = 180° (Fig. 2D), closely matching one nodal plane from the independently determined focal mechanism (strike = 292°, dip = 34°, rake = 177°) (Fig. 2). A secondary peak corresponding to left-lateral strike-slip motion for dip = 35° is tectonically implausible and inconsistent with the P-wave focal mechanism.

Tectonic implications

Figure 2A shows the predicted focal mechanisms for multiple tectonic scenarios, where the fault strike and dip are set by LFE hypocentral alignment, with the rake varied according to that required to accommodate the MORVEL 2010 model plate motions (*39*). We found that the mechanism theoretically predicted by Pacific-Gorda relative plate motions closely matches the computed LFE composite focal mechanism, whereas other tectonic scenarios are outside the range of acceptable solutions (Fig. 2B). Furthermore, the frequent, ~2-day recurrence times observed for this LFE activity would likely be difficult to produce with a low-slip-rate fault, suggesting that they occur on a high-slip-rate fault (*27*), similar to other worldwide observations of plate-bounding tremor and LFEs (*25*). Therefore, we argue that the Mendocino LFEs likely reflect relative motion between the Gorda and Pacific plates.

The determined strike-slip mechanism is inconsistent with the hypothesis that a slab window forms directly south of the Gorda slab in this area. Instead, it suggests that Pacific-like plate motion is actively occurring southeast of the surface expression of the triple junction, beneath the North American plate, matching the hypothesis of capture by the Pacific plate of a partially subducted former Farallon slab fragment (*15*, *17*). We therefore infer that the LFEs reflect slip on an eastward extension of the Mendocino transform fault (Fig. 1).

A puzzling feature noted by Shelly *et al*. (*27*) is that the LFEs occur on the southern edge of an aseismic zone that extends ~15 km south

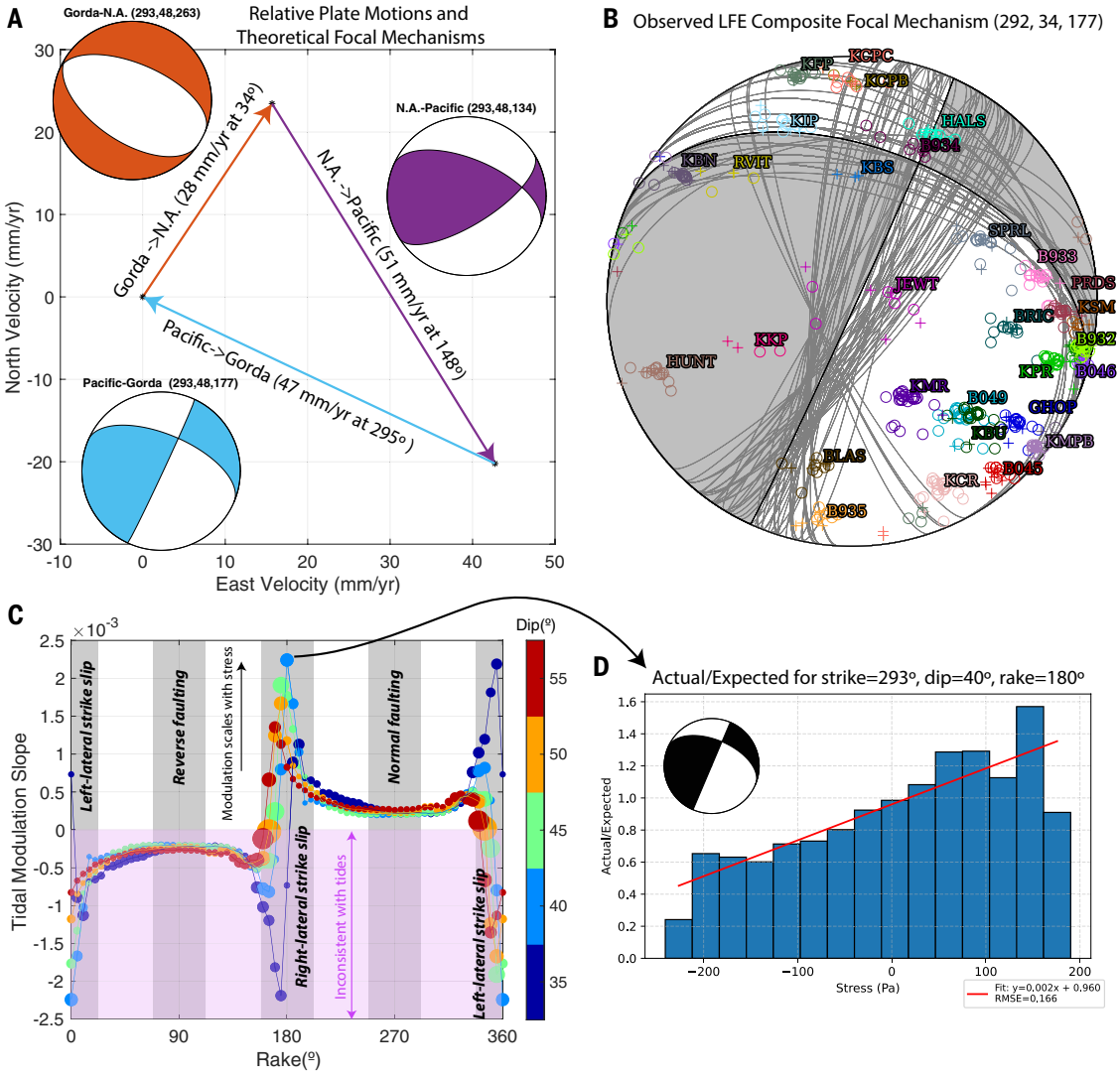

Fig. 2. Comparison of theoretical and determined slip orientations. (**A**) Relative plate motion from the MORVEL 2010 model (*39*) shown with vectors (see the materials and methods). Focal mechanisms corresponding with these relative motions resolved onto the LFE hypocentral plane fit (strike = 293°, dip = 48°) are plotted. Strike, dip, and rake of these mechanisms are indicated above each. (**B**) Composite focal mechanism for all LFE families computed by LFE P-wave polarity analysis. Symbols indicate estimated compressional (plus) or dilatational (circle) polarity observation projected onto the focalsphere labeled with the corresponding station name (corresponding colors). Light lines indicate potential acceptable solutions assuming hypocentral uncertainties of 0.5 km and a 10% polarity error (see the materials and methods). (**C**) Tidal modulation slope for a strike of 293° showing a maximum tidal modulation slope for dip = 40°, rake = 180°. Gray shading shows the range of rake angles corresponding with each faulting type (labeled), with unshaded regions denoting oblique faulting. (**D**) Bar plot showing the ratio of actual to expected event numbers as a function of tidal shear stress for the maximum slope orientation. Bottom inset shows fit and associated root mean squared error (RMSE). Tidal modulation increases systematically with increasing stress. Corresponding mechanism for this orientation is plotted in the inset. Note the close correspondence between the theoretical mechanism representing Pacific-Gorda plate convergence in (A) (light blue) and those determined from P-wave analysis and tidal modulation.

from the southern limit of Gorda slab seismicity (Fig. 3, A and B), with distinctly lower P-wave velocities at ~23 to 30 km depth compared with corresponding depths to the north and (especially) south (*17*, *31*). Although this low-velocity zone is not apparent in seismic refraction data (*11*), perhaps due to limited resolution (figs. S1 and S2), it is prominent in tomography studies and has been previously interpreted as thickened North American crust (*17*, *31*). However, the fault motion of the LFEs implies that rather than being a thickened portion of present-day North American crust, this low-velocity zone is instead accreted to the southern edge of the subducting Gorda slab, shifting the subduction boundary south from the edge of the petrologic slab.

A plausible source of this low-velocity material is the southernmost portion of the North American accretionary prism, which formed as sediments were scraped off the subducting Gorda plate. Figure 3C diagrams our proposed model. Because the western boundary of the accretionary prism (the deformation front) is west of the northward projection of the San Andreas Fault (Fig. 1), the intervening zone is subjected to high rates of north-south compression, more so than the underlying Gorda slab, which is subducting obliquely northeastward relative to North America (Fig. 2A). The Gorda slab has a distinct southward dip at its southern edge, as previously recognized from seismic velocity structure and seismicity (*17*, *31*, *40*) (Fig. 3C). Although the Gorda plate has been previously interpreted from seismic velocity structure as

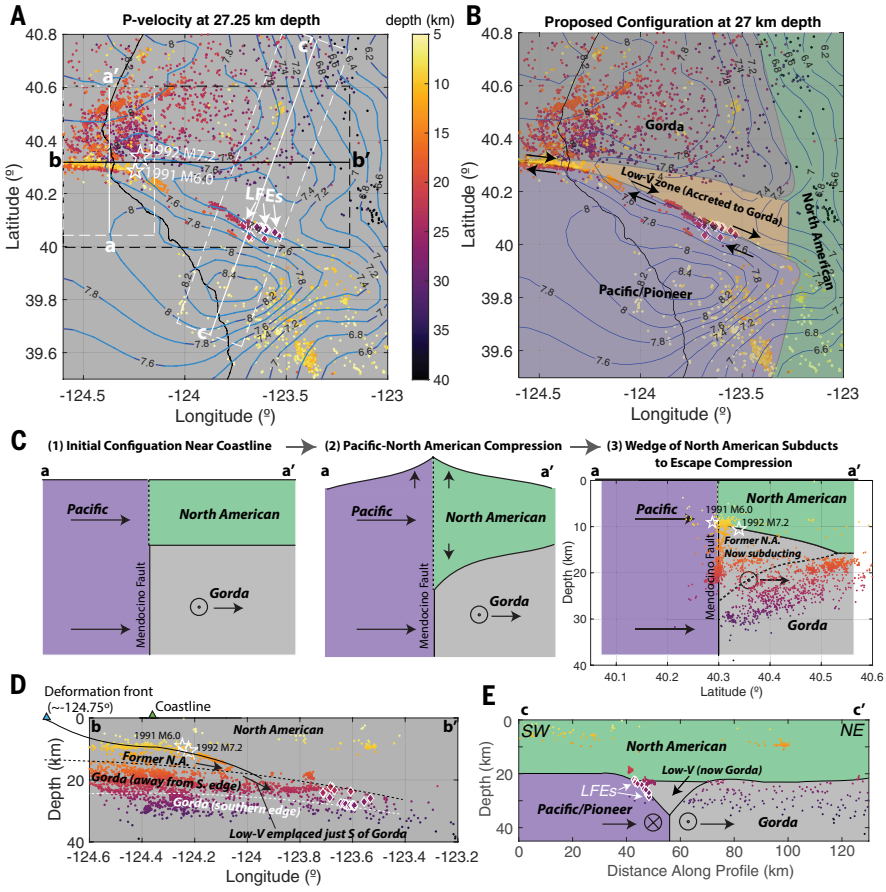

Fig. 3. Velocity structure, seismicity, and proposed formation of the low-velocity zone. Relocated earthquakes and LFEs are from Shelly *et al*. (*27*) and are colored by depth. White stars show the 1991 M 6.0 (Honeydew) and 1992 M 7.2 (Cape Mendocino) thrust-faulting earthquakes, with locations from Waldhauser and Schaff (*72*). (**A**) Contours of P-wave velocity in kilometers per second at 27.25 km depth (near mean depth of LFEs) from Furlong *et al*. (*17*) are shown in blue; note the alignment of LFEs with contours separating a high-velocity zone to the south with the low-velocity zone to the north. Locations of transects shown in (C) to (E) are indicated, with dashed boxes showing regions of plotted seismicity for each. (**B**) Interpreted plate structure at 27 km depth, corresponding with velocity structure. (**C**) Cartoon illustration showing a south-north cross section a to a′ near the coastline, as indicated in (A), with proposed evolution of downwarping at the southern edge of the Gorda slab and progressive subduction of North American accretionary prism to the present-day low-V corridor at the southern edge of the Gorda slab. The circle with a central dot indicates subduction motion of the Gorda plate out of the page. Third panel (at right) overlays actual relocated seismicity. (**D**) West-east cross section b to b′, as indicated in (A), showing shallow seismicity lineation containing the 1991 M 6.0 and 1992 M 7.2 thrust earthquakes projecting to the deformation front, as defined by bathymetry (Fig. 1). We hypothesize that a portion of the former North American (N.A.) accretionary prism subducts above the south-dipping southern edge of the Gorda slab. Dashed black line indicates the approximate upper boundary of Gorda intraslab seismicity, and the white dashed line indicates the same at the Gorda's southern edge. (**E**) Southwest-northeast cross section c to c′ (oriented at 20°) across the LFE zone showing the interpreted structure and the alignment of LFE hypocenters. Arrows indicate approximate motion relative to North America. The circle with a cross indicates motion into the page. Pacific-Gorda relative motion is estimated to be nearly pure strike-slip along the LFE strike.

purely east-dipping beneath the coast (*41*, *42*), a southward dip at its southernmost edge (Fig. 3C) does not conflict with these data (figs. S1 and S3). To escape the compression imparted by the Pacific plate, a portion of accretionary prism above the Gorda slab may have been subducted, effectively transferring these low-velocity sediments back to the Gorda plate from which they originated before accretion onto the continent. This model bears some resemblance to a previously proposed model in which the southernmost portion of the North American accretionary prism was subducted due to eastward migration of the San Andreas Fault and Cascadia subduction front (*43*, *44*). However, we envision this accretionary prism subduction to have occurred progressively as the Mendocino fault moved northward with Pacific plate motion rather than being limited to the time of an eastward jump in the San Andreas Fault. Subduction of this low-velocity zone may continue until it reaches the eastern edge of the Pioneer Fragment and escapes the associated north-south compression east of the observed LFEs (Fig. 3B).

Multiple lines of evidence support the interpretation of a wedge of material subducting above the petrologic Gorda slab at its southern edge. For example, the McCrory *et al*. (*40*) model suggests that the slab is >10 km deep at the southern end of the Cascadia deformation front, implying subduction of a thick layer above the slab (Fig. 1). In addition, repeating earthquakes observed on the Mendocino fault as shallow as ~10 km depth suggest that right-lateral strike-slip motion occurs at slip rates similar to those reflected by repeating earthquakes occurring much deeper (>20 km depth) adjacent to the inferred subducting Gorda slab (*45*).

Further support for this model is provided by the 1992 M 7.2 Cape Mendocino earthquake, which occurred at ~10 km depth and ~10 km above the inferred subducting slab, with low-angle thrust slip consistent with subduction motion (Figs. 1 and 3). Although this event was originally interpreted to represent rupture of the subduction interface (*46*, *47*), more recent studies showing that the rupture was much shallower than the Gorda slab (as reflected by the slab's seismic

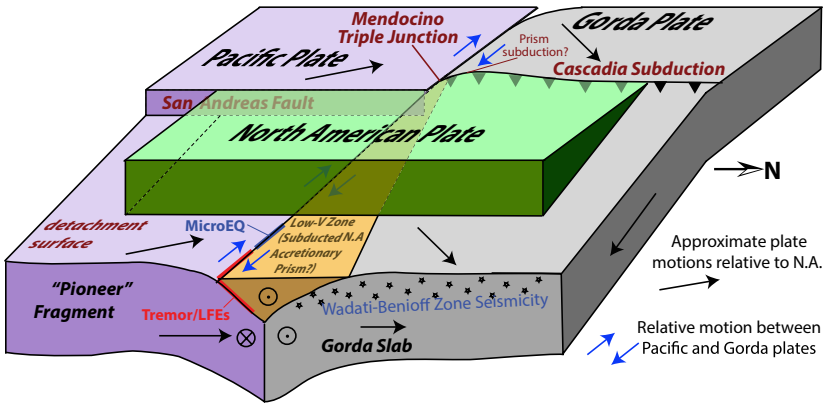

Fig. 4. Proposed plate geometry at the Mendocino triple junction. LFEs are interpreted to occur on the boundary between the captured Pioneer Fragment and a low-velocity zone accreted to the subducting Gorda slab adjacent to a zone of microearthquakes (MicroEQ). Circles with a central dot denote motion out of the page, and the circle with a cross indicates motion into the page. We propose that the low-velocity (low-V) zone is accreted to the Gorda slab and that LFEs occur along the southern boundary of Gorda subduction. A detachment surface with unknown seismic potential likely separates the Pioneer Fragment from the North American crust. LFE motion is nearly pure strike-slip, with the northwesterly strike serving to accommodate north-south compression between the Pacific and Gorda plates (Fig. 2). Diagram view was inspired by Hole *et al*. (*58*).

velocity structure and seismicity) instead interpreted this event as thrusting on a minor fault within the upper plate (*40*, *42*). We infer that the 1992 M 7.2 event occurred on the primary subduction interface fault, and we propose that this interface is ~10 km above the petrologic slab at its southern end, with the depth perhaps influenced by a stress concentration imparted by the upper boundary of thickened lower crust of the colliding Pacific plate (*48*). This interpretation is consistent with the eastward curve of the southernmost offshore deformation front (Fig. 1), which does not project to the slab itself but aligns with the proposed shallower interface and the 1992 M 7.2 rupture (Fig. 3D). This is also consistent with thrust-type mechanisms observed for the 1991 M 6.0 Honeydew earthquake (*49*). The Northern California Seismic System focal mechanism solutions for this event all indicate reverse slip with northeast-dipping (22° to 46°) nodal planes (Fig. 1). A shallow dip is most consistent with potential subduction interface slip. Furthermore, ongoing nearby thrust-type microseismicity extends downdip toward the east (Figs. 1 and 3). This hypothesis effectively reconciles disparate prior interpretations.

Accretionary prisms are well recognized for their considerable fluid content, initially forming from a collection of saturated sediments scraped off the downgoing plate (*50*). As the former accretionary prism subducts, it would be increasingly heated and compressed, likely leading to high fluid pressures, which are strongly associated with tremor and LFE activity and may enable brittle failure under conditions where distributed ductile deformation would otherwise dominate (*51*–*55*). Tremor has been previously observed offshore of Japan within the accretionary prism [e.g., (*56*)], though at somewhat shallower depths than the 22 to 29 km determined for Mendocino LFEs. Alternatively, fluids enabling Mendocino tremor and LFEs could originate from dehydration of the Gorda or Pioneer slabs. Fluids might also contribute to the generation of persistent, sometimes swarm-like microearthquakes (*32*) adjacent to LFE activity. These microearthquakes exhibit diverse focal mechanisms reflecting a combination of strike-slip and normal faulting (Fig. 1), which seems to preclude their occurrence on the same fault as the LFEs. However, their consistent, long-lived activity suggests that they may be associated with tectonic deformation and might reflect fluid-assisted tear faulting immediately above the Pioneer-Gorda boundary. Hybrid shear-dilational faulting associated with high fluid pressure and fracture mesh faulting (*29*, *57*) is also possible.

We present the proposed plate geometry in Fig. 4. The moderately dipping LFE zone suggests that the LFEs may occur along the upper surface of a northward-dipping Pioneer Fragment. If so, despite its northward dip, the Pioneer Fragment is not actively subducting to the north as the southeasterly strike accommodates Pacific-Gorda relative motion (Fig. 2). The proposed geometry is attractive because it is similar to that associated with the main band of tremor and LFEs on the subduction interface in Cascadia (Fig. 1) and elsewhere downdip of the primary seismogenic zone, except that the relative motion in this case is strike-slip rather than thrust.

In this captured slab model, the San Andreas Fault would sole into a shallowly eastward-dipping, midcrustal detachment on the surface of the Pioneer Fragment as it translates northward beneath westernmost North America (*15*, *17*) (Fig. 4). In fact, active-source seismic imaging has resolved a pronounced highly reflective, eastward-dipping structure beneath the northern San Andreas system, although it has been debated whether the San Andreas cuts through this structure (*12*, *58*). The Maacama fault, and possibly the Bartlett Springs fault, would also be expected to sole into this detachment, depending on its eastward extent. Although no associated seismicity on the detachment itself has been reported, the existence of such a structure might impart shear tractions that could help to explain the partitioning of slip across multiple similarly oriented faults of the northern San Andreas system (*17*). Although the detachment might slip aseismically, it alternatively could be capable of generating infrequent, large earthquakes, perhaps extending megathrust rupture from the Cascadia subduction zone itself. Similar lower-crustal structures have been observed farther south in California, leading to a proposal that a midcrustal detachment fault on the surface of a fossil slab may also underlie other portions of the San Andreas Fault system (*59*, *60*) and indeed much of California (*61*). This idea has been revisited more recently (*62*), yet debate continues regarding the prevalence of fossil slabs versus slab windows and asthenospheric upwelling (*13*).

Our results have important implications for subduction zone modeling and seismic hazards. The potentially large discrepancy between petrologic slab boundaries and the faults that accommodate subduction contrasts with usual assumptions that these are practically interchangeable (*40*, *63*). The shallower interface location proposed here, although a small portion of the Cascadia subduction zone, could bring slip closer to the surface and alter slab-coupling or dynamic rupture models, which have relied on the geometry of slab models (*64*, *65*). Perhaps more critically, the proposed detachment fault along the surface of Pioneer Fragment does not appear in current fault models (*66*, *67*) and is not considered in the US Geological Survey National Seismic Hazard Model (*68*). If this fault is seismogenic, then it could represent a substantial unaccounted seismic hazard given the high rate (~51 mm/year) of relative motion between the Pacific and North American plates, exceeding the rate of Gorda subduction (Fig. 2).

The extended length of interaction between the Gorda and Pacific/Pioneer plates at depth onshore might increase the likelihood of interactions between large earthquakes on the Cascadia subduction interface and those along the San Andreas Fault (*69*, *70*). Furthermore, high seismicity rates near the Mendocino triple junction, including three earthquakes of M 6+ since 2021, contrast starkly with the relative seismic quiescence observed throughout most of Cascadia. This may increase the likelihood that the next Cascadia megathrust

earthquake would nucleate within the triple junction, perhaps contributing to an apparently shorter average recurrence interval for southern Cascadia compared with northern Cascadia (*71*). Continued monitoring of tremor and LFEs in this area might help to ascertain any future variations in deep fault slip rate, particularly in the aftermath of neighboring large earthquakes. Such slip variations may be subtle and not detectable by other means.

REFERENCES AND NOTES

1. T. Atwater, *Geol. Soc. Am. Bull.* **81**, 3513–3536 (1970).
2. D. P. McKenzie, W. J. Morgan, *Nature* **224**, 125–133 (1969).
3. K. P. Furlong, S. Y. Schwartz, *Annu. Rev. Earth Planet. Sci.* **32**, 403–433 (2004).
4. E. A. Silver, *Geol. Soc. Am. Bull.* **82**, 2965–2978 (1971).
5. D. S. Wilson, *J. Geophys. Res.* **94**, 3065–3075 (1989).
6. B. Shuck *et al.*, *Sci. Adv.* **11**, eady8347 (2025).
7. G. F. Littel, M. G. Bostock, A. Schaeffer, S. Roecker, *Tectonics* **42**, e2022TC007494 (2023).
8. R. J. Merrill, M. G. Bostock, S. M. Peacock, A. J. Schaeffer, S. W. Roecker, *Geochem. Geophys. Geosyst.* **23**, e2021GC010205 (2022).
9. W. R. Dickinson, W. S. Snyder, *J. Geol.* **87**, 609–627 (1979).
10. B. C. Beaudoin *et al.*, *Geology* **24**, 195–199 (1996).
11. B. C. Beaudoin, J. A. Hole, S. L. Klemperer, A. M. Tréhu, *J. Geophys. Res.* **103**, 30101–30115 (1998).
12. T. J. Henstock, A. Levander, *Geophys. J. Int.* **140**, 233–247 (2000).
13. Z. Yang, D. Zhao, Y. Dong, B. Cheng, *Geol. Soc. Am. Bull.* **137**, 156–166 (2024).
14. G. Zandt, K. P. Furlong, *Geology* **10**, 376–381 (1982).
15. R. G. Bohannon, T. Parsons, *Geol. Soc. Am. Bull.* **107**, 937–959 (1995).
16. K. P. Furlong, J. Lock, C. Guzofski, J. Whitlock, H. Benz, *Int. Geol. Rev.* **45**, 767–779 (2003).
17. K. P. Furlong, A. Villaseñor, H. M. Benz, K. A. McKenzie, *Tectonics* **43**, e2023TC007963 (2024).
18. K. Obara, *Science* **296**, 1679–1681 (2002).
19. K. Obara, H. Hirose, F. Yamamizu, K. Kasahara, *Geophys. Res. Lett.* **31**, 2004GL020848 (2004).
20. G. Rogers, H. Dragert, *Science* **300**, 1942–1943 (2003).
21. M. G. Bostock, A. A. Royer, E. H. Hearn, S. M. Peacock, *Geochem. Geophys. Geosyst.* **13**, 2012GC004391 (2012).
22. W. B. Frank *et al.*, *Geophys. Res. Lett.* **40**, 2661–2666 (2013).
23. D. R. Shelly, G. C. Beroza, S. Ide, *Nature* **446**, 305–307 (2007).
24. D. R. Shelly, J. L. Hardebeck, *Geophys. Res. Lett.* **37**, 2010GL043672 (2010).
25. G. C. Beroza, S. Ide, *Annu. Rev. Earth Planet. Sci.* **39**, 271–296 (2011).
26. A. G. Wech, *J. Geophys. Res. Solid Earth* **126**, e2021JB022523 (2021).
27. D. R. Shelly, D. E. Goldberg, A. G. Wech, A. M. Thomas, *Geophys. Res. Lett.* **52**, e2025GL116116 (2025).
28. S. Ide, D. R. Shelly, G. C. Beroza, *Geophys. Res. Lett.* **34**, 2006GL028890 (2007).
29. D. R. Shelly, J. L. Hardebeck, W. L. Ellsworth, D. P. Hill, *J. Geophys. Res. Solid Earth* **121**, 8622–8641 (2016).
30. D. A. Castillo, W. L. Ellsworth, *J. Geophys. Res.* **98**, 6543–6560 (1993).
31. D. Verdonck, G. Zandt, *J. Geophys. Res.* **99**, 23843–23858 (1994).
32. R. C. McPherson, thesis, California State Polytechnic University, Humboldt, Arcata, CA (1989).
33. R. Nakata, N. Suda, H. Tsuruoka, *Nat. Geosci.* **1**, 676–678 (2008).
34. D. R. Shelly, G. C. Beroza, S. Ide, *Geochem. Geophys. Geosyst.* **8**, 2007GC001640 (2007).
35. A. A. Royer, A. M. Thomas, M. G. Bostock, *J. Geophys. Res. Solid Earth* **120**, 384–405 (2015).
36. J. L. Rubinstein, M. La Rocca, J. E. Vidale, K. C. Creager, A. G. Wech, *Science* **319**, 186–189 (2008).
37. A. M. Thomas, R. M. Nadeau, R. Bürgmann, *Nature* **462**, 1048–1051 (2009).
38. A. M. Thomas, R. Bürgmann, D. R. Shelly, N. M. Beeler, M. L. Rudolph, *J. Geophys. Res. Solid Earth* **117**, 10.1029/2011JB009036 (2012).
39. C. DeMets, R. G. Gordon, D. F. Argus, *Geophys. J. Int.* **181**, 1–80 (2010).
40. P. A. McCrory, J. L. Blair, F. Waldhauser, D. H. Oppenheimer, *J. Geophys. Res. Solid Earth* **117**, 10.1029/2012JB009407 (2012).
41. B. C. Beaudoin, M. Magee, H. Benz, *Geophys. Res. Lett.* **21**, 2319–2322 (1994).
42. H. Guo, J. J. McGuire, H. Zhang, *Nat. Geosci.* **14**, 341–348 (2021).
43. A. Griscom, R. C. Jachens, *J. Geophys. Res.* **94**, 3089–3099 (1989).
44. S. W. Smith, J. S. Knapp, R. C. McPherson, *J. Geophys. Res.* **98**, 8153–8171 (1993).
45. K. Materna, T. Taira, R. Bürgmann, *Geophys. Res. Lett.* **45**, 699–707 (2018).
46. M. H. Murray, G. A. Marshall, M. Lisowski, R. S. Stein, *J. Geophys. Res.* **101**, 17707–17725 (1996).
47. D. Oppenheimer *et al.*, *Science* **261**, 433–438 (1993).
48. T. J. Henstock, A. Levander, *J. Geophys. Res. Solid Earth* **108**, 10.1029/2001JB000902 (2003).
49. R. C. McPherson, *Calif. Geol.* **45**, 31–39 (1992).
50. J. C. Moore, P. Vrolijk, *Rev. Geophys.* **30**, 113–135 (1992).
51. P. Audet, M. G. Bostock, N. I. Christensen, S. M. Peacock, *Nature* **457**, 76–78 (2009).
52. M. Becken, O. Ritter, P. A. Bedrosian, U. Weckmann, *Nature* **480**, 87–90 (2011).
53. Å. Fagereng, G. W. B. Hillary, J. F. A. Diener, *Geophys. Res. Lett.* **41**, 4159–4167 (2014).
54. D. R. Shelly, G. C. Beroza, S. Ide, S. Nakamula, *Nature* **442**, 188–191 (2006).
55. J. R. Delph, A. Levander, F. Niu, *Geophys. Res. Lett.* **45**, 11021–11029 (2018).
56. K. Obana, S. Kodaira, *Earth Planet. Sci. Lett.* **287**, 168–174 (2009).
57. R. H. Sibson, *J. Struct. Geol.* **18**, 1031–1042 (1996).
58. J. A. Hole, B. C. Beaudoin, T. J. Henstock, *Tectonics* **17**, 802–818 (1998).
59. T. M. Brocher *et al.*, *Science* **265**, 1436–1439 (1994).
60. R. Bürgmann, *Geology* **25**, 1135–1138 (1997).
61. T. M. Brocher, U. S. T. E. N. Brink, T. Abramovitz, *Int. Geol. Rev.* **41**, 263–274 (1999).
62. J. E. Pikser, D. W. Forsyth, G. Hirth, *Earth Planet. Sci. Lett.* **331–332**, 315–321 (2012).
63. G. P. Hayes *et al.*, *Science* **362**, 58–61 (2018).
64. K. Materna, J. R. Murray, F. Pollitz, J. R. Patton, *Bull. Seismol. Soc. Am.* **113**, 2505–2518 (2023).
65. M. D. Ramos *et al.*, *J. Geophys. Res. Solid Earth* **126**, JB022005 (2021).
66. A. Plesch, S. Marshall, J. Shaw, "SCEC Community Fault Model (CFM)" (Statewide California Earthquake Center, 2024); https://zenodo.org/records/13685611.
67. K. M. Johnson, W. C. Hammond, R. J. Weldon II, *Bull. Seismol. Soc. Am.* **114**, 1407–1436 (2024).
68. M. D. Petersen *et al.*, *Earthq. Spectra* **40**, 5–88 (2024).
69. C. Goldfinger *et al.*, *Bull. Seismol. Soc. Am.* **98**, 861–889 (2008).
70. C. Goldfinger *et al.*, *Geosphere* **21**, 1132–1180 (2025).
71. C. Goldfinger *et al.*, "Turbidite event history–Methods and implications for Holocene paleoseismicity of the Cascadia subduction zone" (US Geological Survey, Professional Paper No 1661-F, 2012); .
72. F. Waldhauser, D. P. Schaff, *J. Geophys. Res. Solid Earth* **113**, 10.1029/2007JB005479 (2008).
73. W. B. F. Ryan *et al.*, *Geochem. Geophys. Geosyst.* **10**, 2008GC002332 (2009).
74. P. Wessel *et al.*, *Geochem. Geophys. Geosyst.* **20**, 5556–5564 (2019).
75. UC Berkeley Seismological Laboratory, "Northern California Earthquake Data Center" (NCEDC, 2014); https://doi.org/10.7932/NCEDC.
76. D. R. Shelly, "A catalog of low-frequency earthquakes at the southern edge of Cascadia subduction" (US Geological Survey, 2025); https://doi.org/10.5066/P1TCKK7G.

ACKNOWLEDGMENTS

We thank H. Guo for providing a copy of the velocity model from Guo *et al*. (*42*). We greatly appreciate reviews from M. Bostock, J. McGuire, T. Parsons, and R. McPherson and discussions with K. Furlong and J. Watt. Stations used in this study are operated by the US Geological Survey (NC network, https://doi.org/10.7914/SN/NC), UC Berkeley (BK network, https://doi.org/10.7932/BDSN), and the EarthScope Consortium (PB network, https://www.fdsn.org/networks/detail/PB/, last accessed 12 May 2025). Figure 1 was created using GMT6 (*74*). Any use of trade, firm, or product names is for descriptive purposes only and does not imply endorsement by the US Government. **Funding:** This work was supported in part by the National Science Foundation (grant 1848302 to A.M.T.). **Author contributions:** Conceptualization: D.R.S., A.M.T., K.Z.M.; Investigation: D.R.S., A.M.T., R.J.S.; Methodology: D.R.S., A.M.T., R.J.S.; Visualization: D.R.S., A.M.T., R.J.S.; Writing – original draft: D.R.S.; Writing – review & editing: D.R.S., A.M.T., K.Z.M., R.J.S. **Competing interests:** The authors declare no competing interests. **Data, code, and materials availability:** Waveform, phase, and event catalog data were obtained from the Northern California Earthquake Data Center (NCEDC) (*75*) and the EarthScope Seismological Facility for the Advancement of Geoscience (SAGE) Data Management Center (https://ds.iris.edu/ds/nodes/dmc/, last accessed 15 April 2025). The catalog of LFE detections is available from Shelly (*76*). An updated version of the Waldhauser and Schaff (*72*) catalog obtained from https://nocaldd.ldeo.columbia.edu/, last accessed 1 May 2025. Fault information is from the US Geological Survey and the California Geological Survey Quaternary Fault and Fold Database for the United States, accessed 15 May 2025 at: https://www.usgs.gov/natural-hazards/earthquake-hazards/faults. No new materials were generated for this study. All other data needed to evaluate the conclusions in the paper are present in the main text or the supplementary materials.

SUPPLEMENTARY MATERIALS

science.org/doi/10.1126/science.aeb2407
Materials and Methods; Figs. S1 to S5; References (*77–80*)

Submitted 5 August 2025; accepted 20 November 2025

10.1126/science.aeb2407